Duzce University Journal of Science and Technology
Düzce Üniversitesi Bilim ve Teknoloji Dergisi
14 (1), 2026, 130-142.
https://doi.org/10.29130/dubited.1782087
e-ISSN: 2148-2446
https://dergipark.org.tr/en/pub/dubited
Research Article

Effect of CoFe2O4 Addition in the Superconducting and Hardness Characteristics of Bi-2223 Ceramics

Musa Doğruer[1*]

[1] Department of Medical Services and Techniques, Bolu Abant Izzet Baysal University, Bolu, Türkiye. ror.org/01x1kqx83

*Corresponding author: musadogruer@outlook.com

Received: 11.09.2025
Revision: 18.11.2025
Accepted: 01.12.2025
Available Online: 21.01.2026

Abstract: This study investigates the influence of $CoFe_2O_4$ (CFO) content variation (x = 0.000 to 0.010) on the mechanical, structural and superconducting properties of Bi-2223. Vickers microhardness measurements show a clear decrease in hardness with increasing CFO content. This decrease is linked to grain boundary weakening, structural defects, and impurity phases. Multiple hardness models are applied to analyze the indentation size effect (ISE). The Hays-Kendall model provided the closest fit to plateau region. SEM analysis reveals that higher CFO doping leads to increased grain fragmentation, irregular grain shapes, and reduced grain connectivity. Magnetization versus temperature (M–T) measurements are performed. The critical onset temperature (T_c) decreasing from 109.8 K (CFO-0) to 93.4 K (CFO-5) due to enhanced structural disorder and increased magnetic scattering. In summary, the study reveals that adding CFO leads to a decline in both mechanical and superconducting performance of the Bi-2223 samples. This is mainly because of increased grain boundary defects and magnetic scattering.

Keywords: *Bi-2223, $CoFe_2O_4$, ISE, SEM, Magnetization*

I. INTRODUCTION

Superconductivity, discovered in 1911, describes the complete disappearance of electrical resistance and the expulsion of magnetic flux when materials are cooled below a critical temperature (Onnes, 1911). Since its discovery, significant research has focused on identifying and enhancing superconducting materials. These range from simple metals to complex copper-oxide-based compounds, valued for their exceptional electrical and magnetic properties. Among high-temperature superconductors, the $Bi_2Sr_2Ca_2Cu_3O_{10+\delta}$ phase has emerged as particularly promising due to its high critical transition temperature, strong chemical and thermal stability, high current-carrying capacity and resistance to high magnetic fields (Cao et al., 2024; Pham et al., 2024). Despite these advantages, the structure of Bi-2223 ceramics limits their mechanical strength and reliability in practical applications. Several intrinsic challenges, such as weak intergranular coupling, random grain orientations, anisotropic layered structure and sensitivity to external forces, undermine their structural integrity and reduce performance consistency. To address these limitations, ion substitution and addition techniques are employed to improve Bi-2223 superconductors. Metallic (Dogruer, 2022) or rare-earth (Saghafi et al., 2024) dopants enhance grain connectivity, reduce anisotropy, and stabilize the phase, while oxide additives such as $ZnFe_2O_4$ (Tran et al., 2025a) and Fe_3O_4 (Tran et al., 2021) act as flux-pinning centers to increase J_c. Non-magnetic oxides promote phase purity and texture, whereas magnetic oxides further enhance flux pinning but may lower T_c through magnetic scattering.

An important aspect of the mechanical behavior of BSCCO (Bi-2223) materials is the indentation size effect (ISE), which refers to the change in material hardness as a function of indentation. The mechanical properties, including hardness, elasticity and fracture toughness, are vital in various applications, particularly in superconducting magnets and power transmission cables (Sakashita et al., 2010). Thus, exploring the indentation size effect offers valuable insights into how the structure and defect distribution in Bi-2223 materials influence their hardness and mechanical performance (Dogruer et al., 2021; Dogruer et al., 2015). While oxides such as $ZnFe_2O_4$ and Fe_3O_4 have been previously studied as additives in Bi-2223 superconductors, our interest in $CoFe_2O_4$ (CFO) stems from its higher magnetic anisotropy and superior thermal and chemical stability. These properties are advantageous for enhancing flux pinning and preserving phase integrity during high-temperature processing. Importantly, CFO's stronger magnetic characteristics are expected to have a more pronounced impact on both mechanical and superconducting performance of Bi-2223 (Tran et al., 2025a; Tran et al., 2021; Houshiar et al., 2014). Although studies have examined CFO as an additive in superconductors, the influence of CFO doping on the ISE behavior in Bi-2223 ceramics has not yet been reported in the literature. This gap underscores the novelty of the present study.

This report aims to investigate the effect of addition high-purity CFO on the mechanical, structural and superconducting properties of Bi-2223 ceramics. This work includes Vickers microhardness, various models (Meyer's Law, PSR, EPD and HK), SEM imaging and magnetization measurements. Based on these measurements, we evaluate the

This is an open access paper distributed under the terms and conditions of the Creative Commons Attribution-NonCommercial 4.0 International License.

structural degradation, mechanical behavior and superconducting performance of CFO-added Bi-2223. This study contributes to the literature by identifying the most suitable mechanical model (the HK approach). Besides, it focuses on how the addition of CFO influences phase formation (from Bi-2223 to Bi-2212), mechanical integrity and changes in T_c behavior. To the best of our knowledge, this is the first study to comprehensively investigate and model the indentation size effect (ISE) in CFO-added Bi-2223 ceramics.

II. MATERIAL AND METHOD

$CoFe_2O_4$ (CFO) is synthesized via a hydrothermal method using analytical-grade reagents. The starting materials included iron (III) nitrate nonahydrate ($Fe(NO_3)_3{\cdot}9H_2O$), cobalt (II) nitrate hexahydrate ($Co(NO_3)_2{\cdot}6H_2O$), both with a purity of 99%, and 4 M potassium hydroxide (KOH) as the precipitating agent. For the synthesis of $CoFe_2O_4$, an aqueous solution of metal nitrates with a Co/Fe molar ratio of 1:2 is prepared and introduced into a Teflon reaction vessel. This solution undergoes hydrothermal treatment to produce the CFO samples. The KOH solution is added to adjust and maintain the pH at approximately 10 during synthesis, which is conducted at 150 ^oC for 2 h. After synthesis, the resulting precipitate is repeatedly washed with deionized water to remove residual ions and impurities, and subsequently dried at 70 °C. The obtained powder is then ground for 2 h to reduce particle size and obtain nanoscale CFO particles. Bi-2223 is synthesized via the solid-state reaction route. High-purity (99.99%) powders of Bi_2O_3, PbO, $SrCO_3$, $CaCO_3$ and CuO are weighed in stoichiometric ratios, thoroughly mixed, and ground to ensure homogeneity. The resulting mixtures underwent pelletization followed by a four-stage calcination process in air at 670 °C, 750 °C, 800 °C, and 820 °C, each for 48 h. Calcination is carried out in a programmable furnace with controlled heating and cooling rates of 5 °C/min under ambient air conditions. Intermediate grinding and re-pressing are performed between each calcination step to improve phase formation and compositional uniformity (Tran et al., 2018). CFO are then incorporated into the Bi-2223 ceramic according to the nominal composition $(BPSCCO)_{1-x}(CFO)_x$, where x (measured in weight %) = of 0.000, 0.002, 0.004, 0.006, 0.008 and 0.010. The final powders are pelletized at 300 K under atmospheric conditions using an applied pressure of 7000 bar. The mixed powders are thoroughly ground, pressed into pellets and exposed to a sintering process at 850 °C for 168 h in an air atmosphere in the same heating/cooling rates. In the following sections, the samples with varying CFO content are referred to as: CFO-0: (x=0.000), CFO-1: (x=0.002), CFO-2: (x=0.004), CFO-3: (x=0.006), CFO-4: (x=0.008) and CFO-5: (x=0.010).

Vickers microhardness (H_v) measurements are carried out using a Shimadzu HMV-2 microhardness tester with an indentation accuracy of ±0.1 μm. For each sample, measurements are taken from 3 different locations to ensure reliable average values for each applied force. The surface morphology is studied using SEM (scanning electron microscopy). The onset critical temperature (T_c) is obtained by analyzing the M-T curves measured with a 10 Oe applied field, using a Physical Property Measurement System (PPMS, Quantum Design EverCool II).

III. RESULTS AND DISCUSSIONS

In previous work (Tran et al., 2025b), XRD analysis confirmed the coexistence of Bi-2223 and Bi-2212 phases, with the Bi-2223 volume fraction decreasing as the concentration of $CoFe_2O_4$ nanoparticles increased. Resistivity (R–T) measurements showed a monotonic decrease in T_c with nanoparticle addition, whereas J_c evaluation revealed an enhancement at low doping (x = 0.002), indicating improved flux pinning. Magnetization measurements further supported this enhancement and confirmed δl-type pinning as the dominant mechanism. EDX mapping confirmed the incorporation of Co and Fe both within grains and along the grain boundaries. In this study, microhardness, magnetization (M–T) and SEM measurements are performed and analyzed using the same set of samples. SEM images are taken from different surfaces of each sample; therefore, the images presented here differ from those in Ref. (Tran et al., 2025b).

A. Microhardness Characterization

The Vickers hardness values (H_v) across a range of applied forces (0.245 N ≤ F ≤ 2.940 N) are derived through the following relation, providing insight into the material's resistance to indentation under varying forces (Sedky & Salah, 2022).

$$H_v = 1854.4\frac{F}{d^2} \quad (1)$$

here F represents the applied force, and d denotes the measured diagonal length of the indentation. The obtained H_v values at different loads are summarized in Table 1. The H_v parameters are affected by both the CFO concentration and the applied indentation force. The plots of [H_v] versus [F] for all Bi-2223 samples display nonlinear behavior (Fig. 1), exhibiting the characteristic of ISE nature. The H_v values decline with increment of applied force up to 2.000 N, after which they remain nearly constant. A significant change in microhardness is observed as the applied test load increases from

0.245 N to 2.000 N. This indicates the presence of weakly bonded grain boundaries, non-uniform grain orientation and impurity phases. Table 1 shows that the H_v values decrease as CFO content increases, with the CFO-0 sample exhibiting the highest hardness values. At 2.940 N, the maximum hardness value of 1.892 GPa is found for the CFO-0 sample, whereas the smallest value (0.161 GPa) is recorded for the CFO-5 compound. The reduction may be attributed to impurities and irregularities, as confirmed by the SEM analysis. Further, the mechanical performance degradation arises from weak grain boundaries, impurities, cracks and grain misalignment, which disrupt superconducting connectivity. The addition of CFO lowers critical stress, promotes dislocation movement, initiates cracks and accelerates failure (Turkoz et al., 2019).

As shown in Fig. 1, the CFO-0 sample exhibits the highest H_v values and is least affected by increasing forces, indicating superior mechanical performance. As CFO impurity increases, crystallinity deteriorates, grain boundaries become weaker, and structural distortions become more pronounced. SEM analysis supports these findings by showing that the pure sample possesses better crystallographic integrity. In contrast, CFO addition reduces mechanical strength and leads to significant structural and morphological damage. This trend is consistent with XRD results from in Ref. (Tran et al., 2025b), which reveals a reduction in the Bi-2223 phase and an increase in the Bi-2212 phase with increment CFO content.

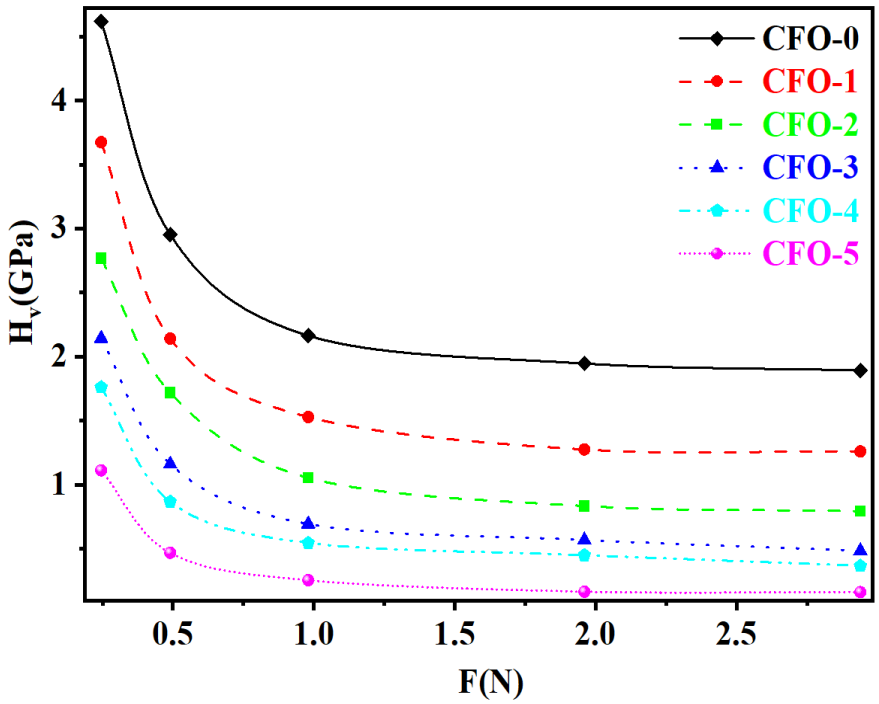


Figure 1. Correlation between hardness (H_v) and applied load (F).

Additionally, the Young's modulus (E), yield strength (Y) brittleness index (B_i), fracture toughness (K_{IC}) and elastic hardness coefficient (C_{11}) are determined by following formulas (Ulgen et al., 2023):

$$E = 81.9635H_V \quad (2)$$

$$Y \approx \frac{H_v}{3} \quad (3)$$

$$B_i = {}^{H_V}/_{K_{IC}} \quad (4)$$

$$K_{IC} = \sqrt{2E\alpha} \quad (5)$$

$$C_{11} = {H_v}^{7/4} \quad (6)$$

The obtained values of E, Y, B_i and K_{IC} are presented in Table 1. Both the load-dependent E and Y values decrease noticeably with increasing CFO content and applied forces. For example, at 0.245 N, E decreases from 378.413 GPa for CFO-0 sample to 91.171 GPa for CFO-5 sample, while Y decreases from 1.538 GPa to 0.370 GPa over the same doping range. This trend is linked to crack initiation and the deterioration of hardness, indicating that the increasing concentration level softens the superconducting material. Moreover, Table 1 shows that K_{IC}, C_{11} and B_i exhibit similar trends to H_v with increasing CFO content and varying applied forces, as these parameters are directly derived from H_v. Therefore, higher H_v values are associated with proportionally higher K_{IC}, C_{11} and B_i values, confirming strong positive correlations between these mechanical properties. In this regard, the highest values of K_{IC}, C_{11} and B_i are observed to be approximately 3.492 Pa/m$^{1/2}$, 14.541 (GPa)$^{7/4}$, and 1.321 m$^{1/2}$ respectively, for the CFO-0 sample at 0.245 N.

Table 1. Numerical values of load-dependent mechanical parameters.

Samples	F *(N)*	H_v *(GPa)*	E *(GPa)*	Y *(GPa)*	K_{IC} *(Pa/m$^{1/2}$)*	B_i *(m$^{1/2}$)*	C_{11} *(GPa)$^{7/4}$*
CFO-0	0.245	4.616	378.413	1.538	3.492	1.321	14.541
	0.490	2.953	242.081	0.984	2.793	1.057	6.654
	0.980	2.163	177.359	0.721	2.390	0.905	3.860
	1.960	1.945	159.481	0.648	2.267	0.858	3.205
	2.940	1.892	155.134	0.630	2.236	0.846	3.054
CFO-1	0.245	3.674	301.148	1.224	3.084	1.191	9.750
	0.490	2.141	175.503	0.713	2.354	0.909	3.790
	0.980	1.528	125.289	0.509	1.989	0.768	2.101
	1.960	1.275	104.510	0.425	1.816	0.701	1.530
	2.940	1.260	103.303	0.420	1.806	0.697	1.499
CFO-2	0.245	2.768	226.929	0.922	2.663	1.039	5.942
	0.490	1.719	140.910	0.573	2.099	0.819	2.581
	0.980	1.053	86.362	0.351	1.643	0.641	1.095
	1.960	0.833	68.327	0.277	1.461	0.570	0.727
	2.940	0.793	65.006	0.264	1.425	0.556	0.666
CFO-3	0.245	2.143	175.657	0.714	2.230	0.960	3.796
	0.490	1.162	95.267	0.387	1.642	0.707	1.301
	0.980	0.693	56.843	0.231	1.268	0.546	0.527
	1.960	0.568	46.617	0.189	1.148	0.495	0.372
	2.940	0.485	39.755	0.161	1.060	0.457	0.281
CFO-4	0.245	1.761	144.377	0.587	1.919	0.917	2.693
	0.490	0.867	71.121	0.289	1.347	0.644	0.780
	0.980	0.546	44.771	0.182	1.068	0.511	0.347
	1.960	0.451	36.975	0.150	0.971	0.464	0.248
	2.940	0.367	30.106	0.122	0.876	0.419	0.173
CFO-5	0.245	1.112	91.171	0.370	1.384	0.803	1.204
	0.490	0.469	38.451	0.156	0.899	0.521	0.265
	0.980	0.254	20.831	0.084	0.661	0.384	0.090
	1.960	0.165	13.580	0.055	0.534	0.310	0.043
	2.940	0.161	13.223	0.053	0.527	0.305	0.041

A. 1. Meyer's Law

Meyer's Law provides a simple and effective method for analyzing the mechanical properties of superconducting materials and is expressed as follows (Hassan et al., 2023).

$$F = A_1{}^n \tag{7}$$

where A_1 is the standard hardness constant and n is the Meyer number. The value of n is obtained from the slope of Fig. 2, while the A_1 is evaluated from the vertical intercept of the curve. The parameter n is crucial for evaluating the ISE and reverse ISE (RISE) behavior. When $n < 2$, microhardness decreases with increasing load, indicating typical ISE behavior. When $n > 2$, hardness increases with force, reflecting RISE behavior. At $n = 2$, the material follows Kick's law, where the applied load is proportional to the square of the indentation diagonal (d^2), expressed as $F = A_1 d^2$. As shown in Table 2, the n values decrease with increasing $CoFe_2O_4$ concentration and remains below 2 for all samples, indicating ISE behavior. The maximum n value (1.467) is obtained for the CFO-0 sample, whereas the minimum (1.108) is observed for CFO-5. The high linear regression coefficient (*LRC*) values for all samples indicate that Eq. (7) accurately fits the indentation data. These results indicate that the CFO-5 sample is the most sensitive to the applied force, likely because of enhanced structural defects. In contrast, the pure sample demonstrates the greatest resistance to loading, owing to its enhanced stiffness, mechanical durability and overall strength (Turkoz et al., 2019).

Table 2. The *n* and ln(*A*) values for CFO-doped Bi-2223 ceramic.

Samples	A_1 *(N/μm²)*	n	LRC
CFO-0	-4.853	1.467	0.99638
CFO-1	-4.842	1.390	0.99538
CFO-2	-4.808	1.312	0.99728
CFO-3	-4.833	1.252	0.99672
CFO-4	-4.934	1.238	0.99601
CFO-5	-4.829	1.108	0.99455

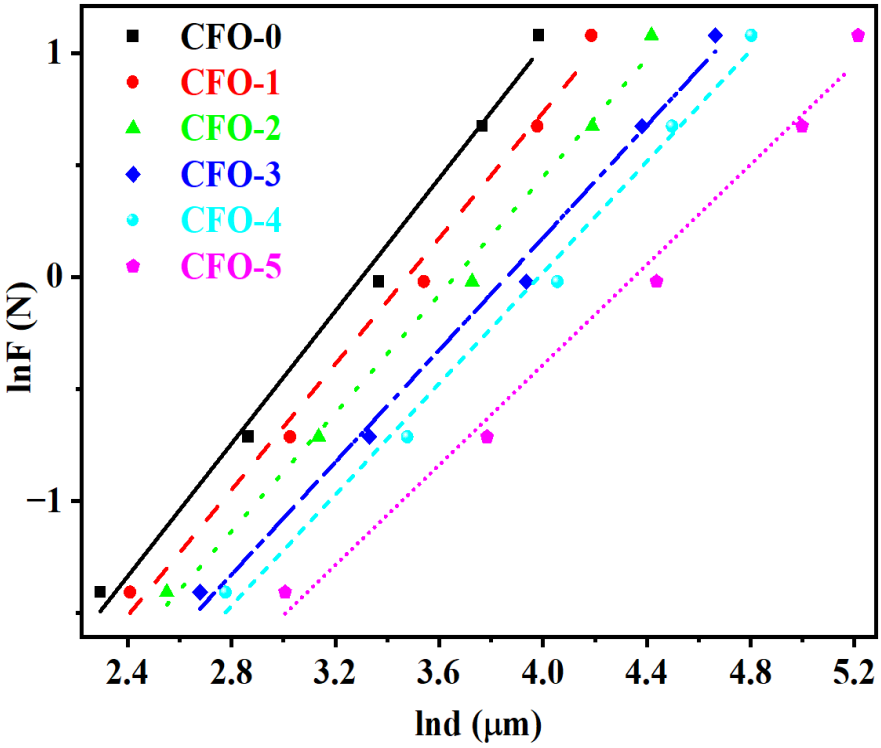


Figure 2. Change of applied load (*lnF*) vs. diagonal (*lnd*) for the sample.

A.2. Proportional Sample Resistance (PSR) Model

The PSR model is commonly used to characterize the ISE nature in superconducting material and is expressed by the following equation (Matar et al., 2025):

$$F/d = \alpha + \beta d \qquad (8)$$

where α presents surface energy and β is the hardness parameter. The load-independent hardness (H_{PSR}) is calculated from β using the relation $H_{PSR}=1854.4\ \beta$. The values of α and β, found from the intercept and slope of Fig. 3, are demonstrated in Table 3. Although the *LRC* values decrease with increasing CFO concentration, the value for the CFO-5 sample is found to be 0.84957. However, the reduction in *LRC* reveals that the PSR model becomes less reliable for predicting true hardness at greater CFO concentration. As demonstrated in the Table 3, the α values are positive for all compounds, indicating the presence of ISE characteristic. Both α and β values decrease with increasing concentration, with the maximum values observed for the CFO-0 sample and the minimum values for the CFO-5 sample. This deterioration is attributed to non-recoverable stress amplification, granularity, weak grain boundaries, irreversible crystal structure, cracking, and uneven grain orientation (Hays & Kendall, 1973; Bilgili et al., 2008). Additionally, as shown in Table 3 show that the PSR model does not accurately predict the true microhardness, as the H_{PSR} values are lower than those in the saturation region.

Table 3. Values of *α, β, LRC, H_{PSR},* and H_v in the plateau region for CFO-doped Bi-2223 phase.

Samples	αx10^{-2} *(N/μm)*	β x10^{-4} *(N/μm²)*	LRC	H_{PSR} *(GPa)*	Hv *(GPa)*
CFO-0	1.611	6.913	0.99093	1.281	1.892–1.945
CFO-1	1.579	4.137	0.98614	0.767	1.260–1.275
CFO-2	1.563	2.254	0.98711	0.418	0.793–0.833
CFO-3	1.415	1.250	0.98335	0.231	0.485–0.568
CFO-4	1.276	0.930	0.97549	0.172	0.367–0.451
CFO-5	1.051	0.239	0.84957	0.044	0.161–0.165

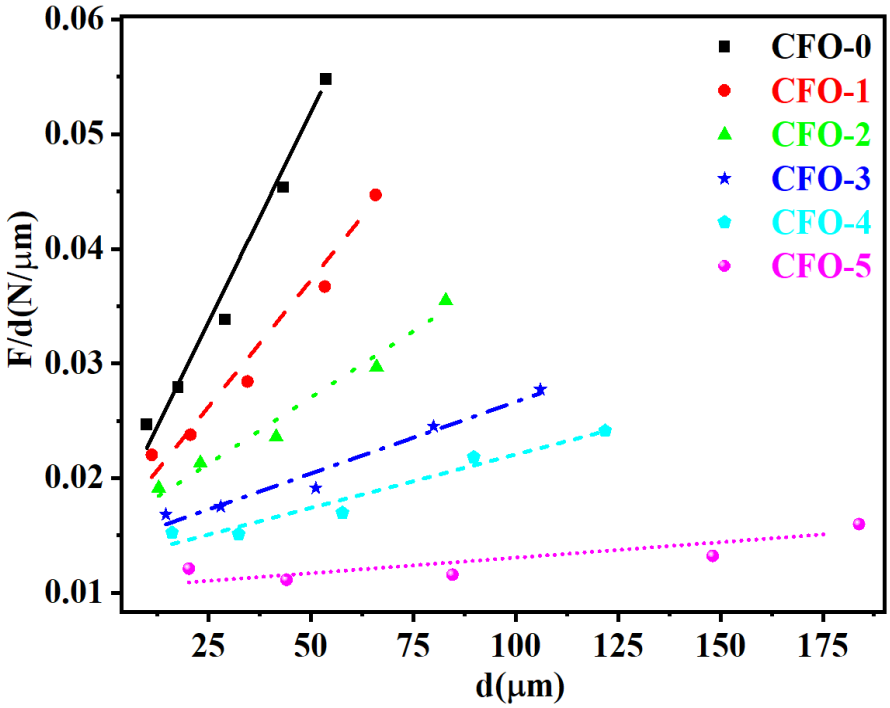


Figure 3. Plots of *F/d* versus *d* for the samples.

A.3. Elastic and Plastic Deformation (EPD) Model

Based on the elastic-plastic deformation (EPD) model, Eq. (9) describes the relationship between applied loads and effective notch size (Ozturk et al., 2018):

$$F = A_2(d_e + d_p)^2 \quad (9)$$

Here, A_2 is a constant, and d_e is related to d_p (plastic deformation), as detailed in Table 4. The variation of indentation diagonal length with applied load is shown in Fig. 4. Table 4 indicates that each graph demonstrates a strong linear correlation, with *LRC* values ≥ 0.99878. All samples exhibit the ISE characteristic, as the d_e values are positive. The load-independent microhardness (H_{EPD}) is computed from the constant A_2 using the relation $H_{EPD}=1854.4A_2$. The maximum A_2 and H_{EPD} parameters are approximately 7.713 × 10^{-4} (N/μm^2) and 1.430 GPa, respectively, for the CFO-0 sample. The lowest values, A_2 = 0.523 × 10^{-4} (N/μm^2) and H_{EPD} = 0.097 GPa, are found for the CFO-5 sample, as shown in Table 4.

Table 4. Values of d_e, A_2, *LRC*, H_{EPD} and H_v in the plateau region for CFO-Doped Bi-2223 Phase.

Samples	d_e *(μm)*	A_2 x10^{-4} *(N/μm²)*	LRC	H_{EPD} *(GPa)*	Hv *(GPa)*
CFO-0	0.208	7.713	0.99950	1.430	1.892–1.945
CFO-1	0.240	4.883	0.99945	0.905	1.260–1.275
CFO-2	0.286	2.922	0.99954	0.541	0.793–0.833
CFO-3	0.313	1.779	0.99952	0.330	0.485–0.568
CFO-4	0.320	1.355	0.99903	0.251	0.367–0.451
CFO-5	0.364	0.523	0.99878	0.097	0.161–0.165

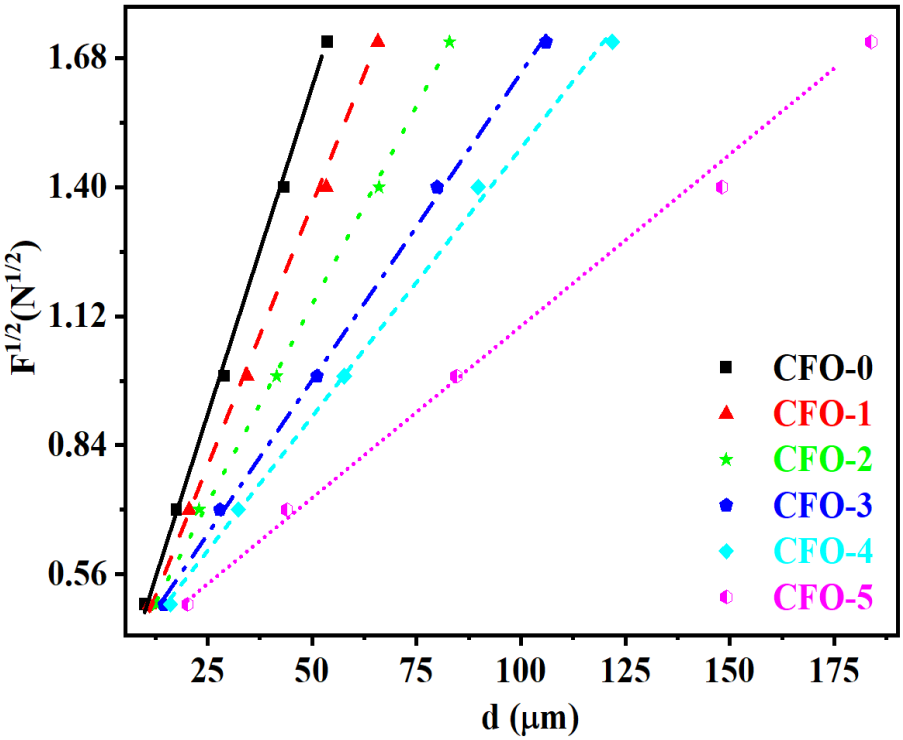


Figure 4. Correlation between square root of applied loads and diagonal length in the samples.

A.4. Hays-Kendall (HK) Approach

The indentation size effect (ISE) observed in microhardness testing shows that materials differently to varying loads. Below a certain threshold, only elastic deformation occurs, but above this threshold, plastic deformation begins suddenly. When the applied load surpasses a critical value, the indenter begins to penetrate further into the material. However, this penetration is influenced not only by the applied load but also by an effective load (F_{eff}), which incorporates the material's hardness constant (W_{HK}). The relationship between indentation size and the applied force is described by the equation (Dogruer et al., 2024):

$$F_{eff} = F - W_{HK} = A_3 d^2 \quad (10)$$

here, A_3 is a constant. The load-independent hardness (H_{HK}) is determined using $H_{HK}=1854.4A_3$. The parameters A_3, LRC and W_{HK} can be determined from the graph of [F] versus [d^2] as shown in Fig. 5. The corresponding A_3, W_{HK}, LRC and H_{HK} values are displayed in Table 5. The high LRC values across all samples indicate that Eq. (10) effectively represents the indentation data. Furthermore, the A_3 values decrease, while the W_{HK} parameters increase with the addition of CFO concentration. The positive W_{HK} values observed in all samples confirm the presence of ISE phenomena. This is because the applied load is adequate to induce both plastic and elastic deformation in the samples. Compared to the other models, the HK model produced values closest to the plateau region, making the HK approach the most suitable model for representing the mechanical properties. While all models confirmed the presence of ISE in CFO-added Bi-2223, their accuracy varied. EPD showed good trend correlations according to PSR, and the PSR model is unsuitable due to poor agreement with experimental results. In conclusion, the HK model yielded hardness values most closely fitting the plateau region, making it the most accurate and reliable model for describing the mechanical behavior of these superconductors (Turkoz et al., 2019). Besides, Fig. 6 shows H_v at 2.940 N and all models (PSR, EPD, and HK) against the concentration level. When comparing the PSR, EPD and HK models, it is evident that the HK model is the closest to the Hv at 2.940 N, making it the most accurate approach. Fig. 6 clearly shows that the HK model aligns most closely with the plateau value.

Table 5. W_{HK}, A_3, *LRC*, H_{HK} and H_v values in the plateau region for CFO-doped Bi-2223 ceramics.

Samples	W_{HK} *(N)*	A_3 x10^{-4} *(N/μm²)*	LRC	H_{HK} *(GPa)*	H_V *(GPa)*
CFO-0	0.171	9.660	0.99990	1.791	1.892–1.945
CFO-1	0.199	6.303	0.99959	1.168	1.260–1.275
CFO-2	0.249	3.930	0.99912	0.728	0.793–0.833
CFO-3	0.293	2.424	0.99673	0.449	0.485–0.568
CFO-4	0.309	1.840	0.99454	0.341	0.367–0.451
CFO-5	0.312	0.774	0.99737	0.143	0.161–0.165

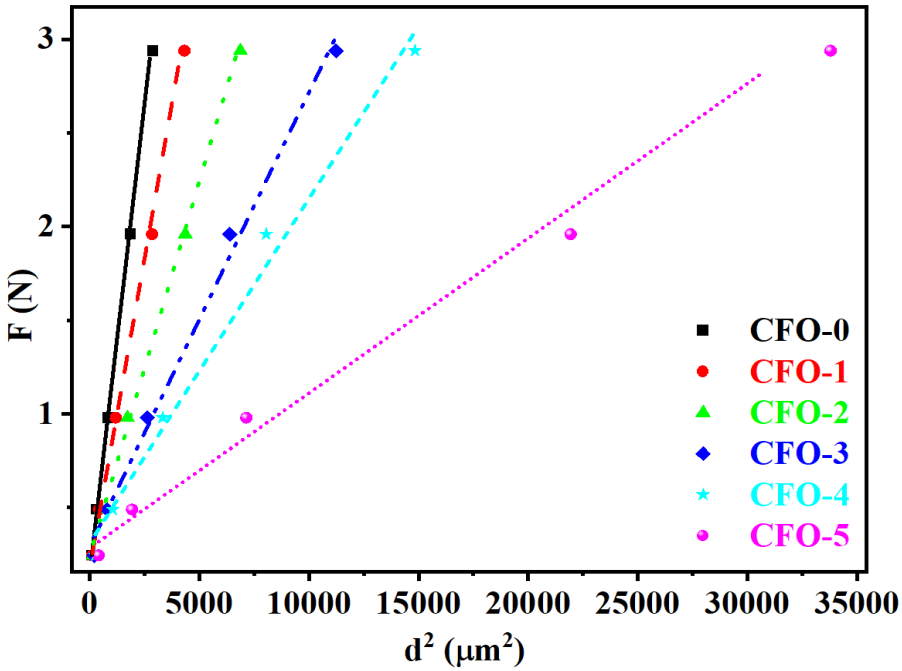


Figure 5. Graph of applied load versus the square of the indentation length.

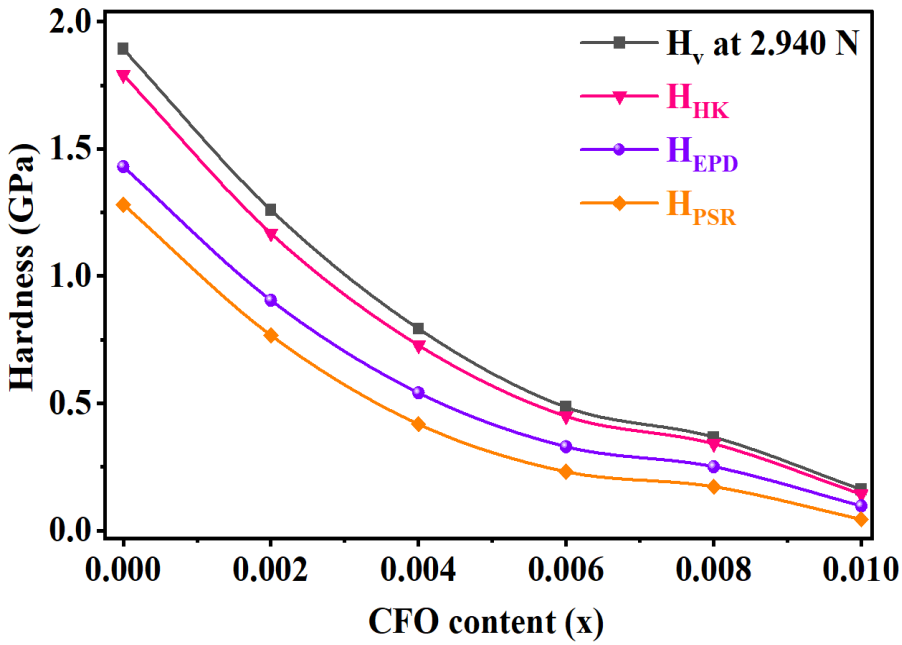


Figure 6. Dependence of (H_v at 2.940 N, H_{PSR}, H_{EPD} and H_{HK}) with concentration level.

B. SEM Analysis and Corresponding Grain Size Distributions

The SEM micrographs in Fig. 7 illustrate the morphological evolution of the superconducting samples with varying concentrations of CFO. All images are captured at 5000× magnification with a 10 μm scale bar. In the CFO-0 sample, the microstructure is dominated by well-developed, plate-like grains characteristic of the Bi-2223 phase, exhibiting smooth surfaces and good crystalline quality. This plate-like morphology remains predominant in the CFO-1 sample. As the CFO concentration level increases to CFO-2 and CFO-3, the microstructure becomes more heterogeneous, presenting the fragmented grains. For CFO-4 and CFO-5 samples, needle-like grains become more prominent, indicating a significant change in the microstructural growth mechanism. The CFO-4 sample exhibits dense grain growth and a wide size distribution, suggesting accelerated grain coarsening at this concentration. These morphological variations are consistent with the concentration-dependent effect of CFO on sintering behavior. The emergence of elongated grains at higher CFO levels suggests suppression of the Bi-2223 phase and a compositional shift toward Bi-2212 formation. This interpretation agrees with earlier XRD results on the same samples, which showed a decreasing Bi-2223 volume fraction and an increasing Bi-2212 fraction with rising CFO content (Tran et al., 2025a). The observed microstructural evolution, from plate-like to more elongated grains, thus confirms the phase transformation shown by XRD (Tran et al., 2025b). The grain size distribution obtained from the Fig. 8 also provides this trend. The CFO-0 sample shows a broad size distribution ranging from ~2 to 16 μm, with most grains concentrated in the 10–14 μm range. CFO-1 sample exhibited a narrower distribution with most grains between 3 and 7 μm and a peak frequency around 5 μm, along with a few larger grains (~12 μm). CFO-2 and CFO-3 samples are characterized by fine grains predominantly in the 1–4 μm range, with CFO-3 showing a slightly narrower distribution compared to CFO-2. In contrast, CFO-4 showed a wide distribution (4–16 μm) with a significant population of coarse grains between 10–14 μm, confirming extensive grain growth. CFO-5 presented an intermediate case with grains primarily distributed between 3 and 7 μm, with occasional larger grains (~10 μm). In conclusion, these results indicate that increasing CFO concentration significantly affects the grain morphology, distribution, and phase stability of Bi-2223 ceramics.

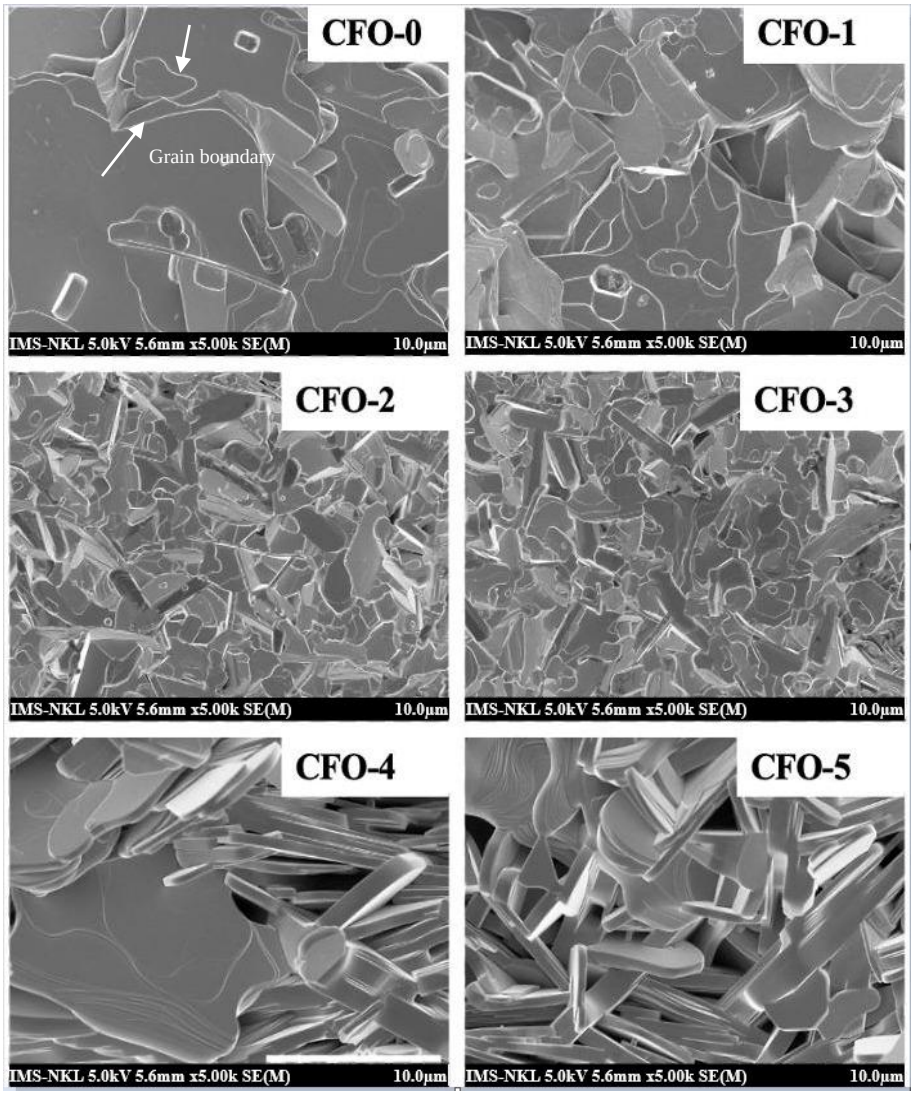


Figure 7: The SEM images of Bi-2223 samples with CFO addition.

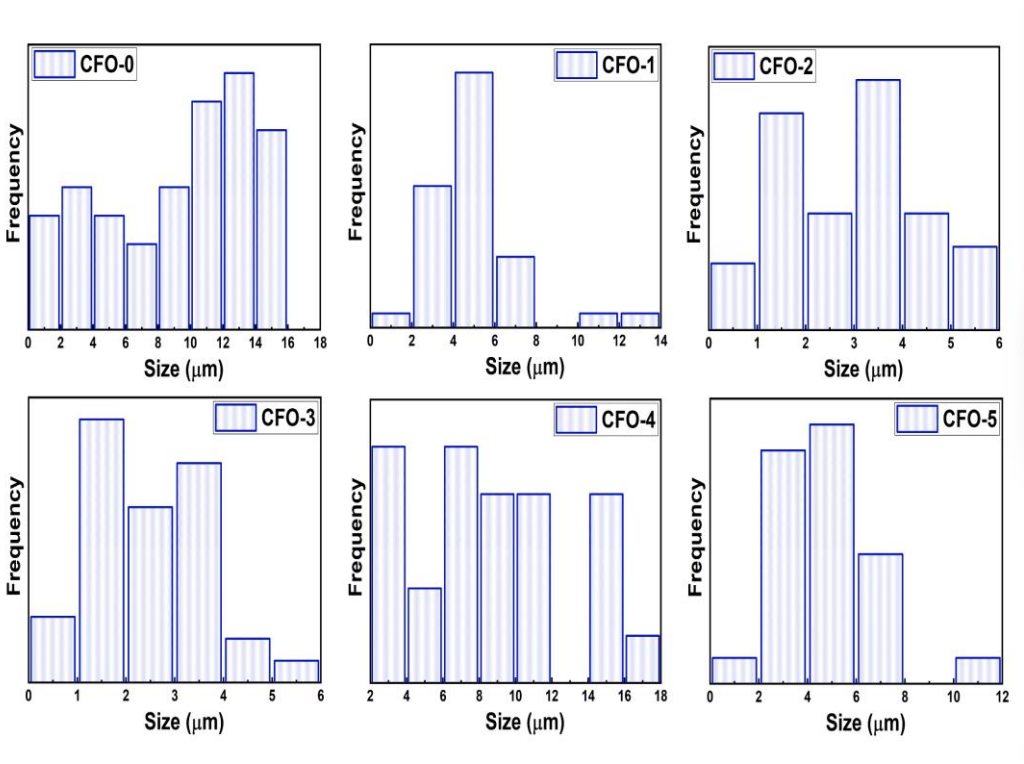


Figure 8: Grain size distributions for each sample are illustrated in the corresponding histograms.

C. Temperature-Dependent Magnetization

Magnetization-temperature (M–T) measurements under an applied magnetic field of 10 Oe are carried out to evaluate the samples, as presented in Fig. 9. All samples display a diamagnetic transition characteristic of superconductivity. The onset critical temperatures (T_c) decrease with increasing CFO concentration, with values of 109.8 K for CFO-0, 109.1 K for CFO-1, 104.4 K for CFO-2, 98.85 K for CFO-3, 96.65 K for CFO-4, and 93.4 K for CFO-5. This decrease indicates a gradual deterioration of the superconducting phase, likely caused by structural disorder, impurity-phase formation and enhanced scattering centers introduced by the magnetic CFO particles (Dogruer et al., 2024). The inset of Fig. 9 highlights variations in the diamagnetic onset of and sharpness of the transition. The CFO-0 sample exhibits the sharpest transition and strongest diamagnetic response, confirming high phase purity and good grain connectivity. In contrast, the CFO-5 sample demonstrates a broadened transition, indicating poor intergranular coupling and the presence of non-superconducting regions. The observed suppression of superconductivity with increasing CFO content may be attributed to the magnetic or impurity phases that disrupt the Cu–O planes, causing electron scattering and lattice distortions that reduce T_c. These results align with a similar trend observed in Bi-2223 systems with the addition of oxides such as $ZnFe_2O_4$ (Tran et al., 2025a), Fe_3O_4 (Tran et al., 2021), SnO_2 (Vu et al., 2023) where T_c values decrease as the amount added increases. Although, low CFO content may still allow acceptable superconducting performance, especially in applications like magnetic levitation or superconducting magnets, where improved flux pinning is beneficial. However, at higher concentrations, CFO causes significant performance loss due to magnetic scattering and structural weakening (Tran et al., 2025b; Salem et al., 2018).

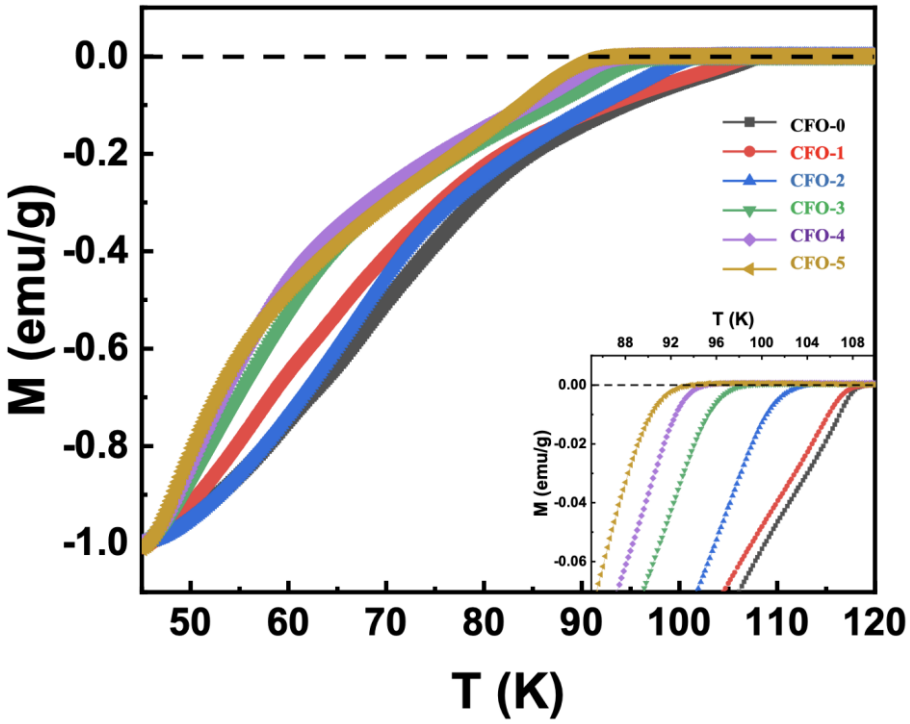


Figure 9: Magnetization as a function of temperature for Bi-2223 materials with CFO addition.

IV. CONCLUSION

- This The H_v values decreased significantly with increasing CFO content. At a force of 0.245 N, the CFO-0 sample showed the highest hardness value of 4.616 GPa, while the CFO-5 sample exhibited the lowest hardness of 1.112 GPa.
- At a load of 2.940 N, the E values showed a noticeably decrease with CFO addition, dropping from 155.134 GPa for sample CFO-0 to 13.223 GPa for sample CFO-5. This reduction is attributed to the increase in impurity phases.
- Y values at 2.940 N decreased from 0.630 GPa in CFO-0 to 0.053 GPa in CFO-5, indicating a substantial weakening of the ability of material to resist plastic deformation. K_{IC} values at 0.245 N decreased from 3.492 Pa/m$^{1/2}$ for the pure sample to 1.384 Pa/m$^{1/2}$ for the CFO-5 sample, demonstrating the negative effect of crack propagation.
- B_i values at 0.245 N declined from 1.321 m$^{1/2}$ in the pure sample to 0.803 m$^{1/2}$ in CFO-5, supporting the reduced structural stability. C_{11} values at 0.245 N showed decrease, from 14.541 (GPa)$^{7/4}$ in CFO-0 to 1.204 (GPa)$^{7/4}$ in CFO-5, reinforcing the observed degradation in mechanical integrity.
- Meyer's law, PSR and EPD models showed reasonable correlation but less accurate than the HK model.
- The HK model effectively described the load-independent hardness behavior by providing the best fit for the plateau region, making it the most suitable model.
- SEM analysis revealed a morphological shift from plate-like Bi-2223 grains in the pure sample to needle-like Bi-2212 grains in the CFO-5 sample, while grain size analysis highlights the strong influence of synthesis conditions on grain growth and distribution across the CFO samples.
- The T_c decreased from 109.8 K (CFO-0) to 93.4 K (CFO-5) as the CFO content increased. This trend indicates a reduction in superconducting phase purity, likely due to the introduction of inclusions that enhance magnetic and electronic scattering.

This study provides valuable insights into how the mechanical and superconducting properties of Bi-2223 superconductors are affected by the addition of CFO and suggests that low CFO concentrations may enable useful applications, while higher concentrations can lead to significant performance degradation. The findings also highlight the significance of modeling approaches such as the HK model to accurately define the indentation behavior of this material.

DECLARATIONS

Acknowledgements: The author expresses gratitude to Dr. D. Hai Tran of the University of Hanoi, Vietnam, for providing the CFO-doped Bi-2223 samples.

Author Contributions: All parts of the study were conducted by the Author.

Conflict of Interest: The author declares no conflict of interest.

Supporting Institutions: This research received no external funding.

Ethical Approval: This study does not involve human or animal participants. All procedures followed scientific and ethical principles, and all referenced studies are appropriately cited.

Plagiarism Statement: This article has been evaluated for plagiarism and no instances of plagiarism were detected.

Data Availability: Data sharing is not applicable to this study.

Use of AI Tools: The author declare that no Artificial Intelligence (AI) tools were used in the creation of this article.

REFERENCES

Bilgili, O., Selamet, Y., & Kocabas, K. (2008). Effects of Li substitution in Bi-2223 superconductors. *Journal of Superconductivity and Novel Magnetism, 21*, 439–449. https://doi.org/10.1007/s10948-008-0374-4

Cao, H., Zhang, S., Cui, Y., Zhi, L., Zhang, Y., Zhang, W., Liu, X., Liu, J., Li, C., & Zhang, P. (2024). Development of a novel fabrication technique for high-quality Bi-2223 bulks with high superconducting performance. *Ceramics International, 50*(7), 12212–12221. https://doi.org/10.1016/j.ceramint.2024.01.125

Dogruer, M. (2022). Influence of Fe/Ca substitute on fundamental properties of $Bi_{1.8}Pb_{0.35}Sr_{1.9}Ca_{2.2-x}Fe_xCu_3O_y$ materials. *Journal of Alloys and Compounds, 900*, Article 163445. https://doi.org/10.1016/j.jallcom.2021.163445

Dogruer, M., Aksoy, C., Yildirim, G., Ozturk, O., & Terzioglu, C. (2021). Influence of Sr/Nd partial replacement on fundamental properties of Bi-2223 superconducting system. *Journal of Materials Science: Materials in Electronics, 32*, 7073–7089. https://doi.org/10.1007/s10854-021-05417-4

Dogruer, M., Motoki, T., Semba, M., Nakamura, S., & Shimoyama, J. (2024). Mechanical properties of Ag-added $DyBa_2Cu_3O_y$ superconducting melt-textured bulks prepared by the single-direction melt growth method. *Materials Today Communications, 39*, Article 108605. https://doi.org/10.1016/j.mtcomm.2024.108605

Dogruer, M., Terzioglu, C., Yildirim, G., Pakdil, M., & Zalaoglu, Y. (2015). Decrement of crack propagation in bulk Bi-2223 superconducting ceramics with Sn-diffusion annealing temperature. *Journal of Materials Science: Materials in Electronics, 26*, 6013–6019. https://doi.org/10.1007/s10854-015-3177-y

Hassan, M. S., Mohamed, I. E., Matar, M., Abou-Aly, A. I., Awad, R., & Anas, M. (2023). Effect of hard magnetic ferrite ($Ba_{0.5}Sr_{0.5}Fe_{12}O_{19}$) nanoparticles on the mechanical properties of the (Bi, Pb)-2223 phase. *Applied Physics A*, *129*, Article 333. https://doi.org/10.1007/s00339-023-06557-6

Hays, C., & Kendall, E. G. (1973). An analysis of Knoop microhardness. *Metallography, 6*, 275–282. https://doi.org/10.1016/0026-0800(73)90053-0

Houshiar, M., Zebhi, F., Razi, Z. J., Alidoust, A., & Askari, Z. (2014). Synthesis of cobalt ferrite ($CoFe_2O_4$) nanoparticles using combustion, coprecipitation, and precipitation methods: A comparison study of size, structural, and magnetic properties. *Journal of Magnetism and Magnetic Materials*, *371*, 43–48. https://doi.org/10.1016/j.jmmm.2014.06.059

Matar, M., Najem, A., Habanjar, K., Anas, M., & Awad, R. (2025). Mechanical properties of $(Ba_{0.4}Sr_{0.4}Ca_{0.2}Fe_{12}O_{19})_x$/($Bi_{1.6}$, $Pb_{0.4}$)-2223 composite impacted in seawater. *Applied Physics A, 131*, Article 110. https://doi.org/10.1007/s00339-024-08196-x

Onnes, H. K. (1911). Further experiments with liquid helium. D. On the change of electrical resistance of pure metals at very low temperatures, etc. V. The disappearance of the resistance of mercury. *KNAW Proceedings, 14*, 113–115. https://dwc.knaw.nl/DL/publications/PU00013124.pdf

Ozturk, O., Asikuzun, E., Tascı, A. T., Gokcen, T., Ada, H., Koralay, H., & Cavdar, S. (2018). Comparison of Vickers microhardness of undoped and Ru doped BSCCO glass ceramic materials. *Journal of Materials Science: Materials in Electronics, 29*, 3957–3966. https://doi.org/10.1007/s10854-017-8336-x

Pham, A. T., Le, T., Hong, V. T. A., Lee, H., Park, T., Thien, N. D., Anh, D. T. K., Nam, N. H., Binh, N. T., Man, N. K., Thao, P. N., Hop, D. T. B., Miyanaga, T., Pham, Q. N., & Tran, D. H. (2024). Vortex phase diagram and transition in $(Bi_{1.6}Pb_{0.4}Sr_2Ca_2Cu_3O_{10-\delta})_{1-x}(SnO_2)_x$ superconductors. *Results in Physics, 63*, Article 107887. https://doi.org/10.1016/j.rinp.2024.107887

Saghafi, M., Shams, G., & Soltani, Z. (2024). Paraconductivity in $Bi_{1.6}Pb_{0.4}Sr_2Ca_2Cu_3O_{10+\delta}$ superconductors doped with Sm_2O_3 nanoparticles. *Physica B: Condensed Matter, 678,* Article 415754. https://doi.org/10.1016/j.physb.2024.415754

Sakashita, T., Ito, S., & Hashizume, H. (2010). Improvement of joint structure for mechanical butt joint of stacked BSCCO 2223 cable. *IEEE Transactions on Applied Superconductivity*, *20*(3), 1751–1754. https://doi.org/10.1109/TASC.2010.2043660

Salem, M. K. B., Slimani, Y., Hannachi, E., Azzouz, F. B., & Salem, M. B. (2018). Bi-based superconductors prepared with addition of $CoFe_2O_4$ for the design of a magnetic probe. *Cryogenics*, *89*, 53–57. https://doi.org/10.1016/j.cryogenics.2017.11.005

Sedky, A., & Salah, A. (2022). Comparative study of the effects of La-substituted Ca in (Bi, Pb):2212 and (Bi, Pb):2223 superconductors. *Journal of Electronic Materials, 51*, 3042–3058. https://doi.org/10.1007/s11664-022-09476-z

Tran, D. H., Le, T. M., Do, T. H., Dinh, Q. T., Duong, N. T. T., Anh, D. T. K., Man, N. K., Pham, D., & Kang, W. N. (2018). Enhancements of critical current density in the Bi–Pb–Sr–Ca–Cu–O superconductor by Na substitution. *Materials Transactions*, *59*(7), 1071–1074. https://doi.org/10.2320/matertrans.MD201715

Tran, D. H., Pham, A. T., Binh, N. T., Anh, D. T. K., Nam, N. H., Hong, N. T. M., Cuong, L. V., Pham, P. V., Huy, N. Q., Huong, T. T., Man, N. K., Lim, K. P., Kechik, M. M. A., Chen, S. K., & Le, T. (2025b). Superconductivity in $Bi_{1.6}Pb_{0.4}Sr_2Ca_2Cu_3O_{10+\delta}$ ceramics with cobalt ferrite ($CoFe_2O_4$) nanoparticle addition. *Ceramics International*, *51*(12), 16134–16142. https://doi.org/10.1016/j.ceramint.2025.01.451

Tran, D. H., Pham A. T., Nam, N. H., Thuy, K. X., Truong, A. D., Le, T., Le, V. C., Hong, N. T. M., Hai, P., Hop, D. T. B., & Dogruer, M. (2025a). Effect of $ZnFe_2O_4$ addition on the phase stability, hardness and superconducting properties of Bi-2223 phase. *Ceramics International*, *51*(20), 30974–30983. https://doi.org/10.1016/j.ceramint.2025.04.289

Tran, D. T., Pham, A. T., Pham, H. H., Nguyen, N. T., Nam, N. H., Man, N. K., Kang, W. N., Hsu, I. J., Klysubun, W., & Tran, D. H. (2021). Local structure and superconductivity in $(Bi_{1.6}Pb_{0.4}Sr_2Ca_2Cu_3O_{10+\delta})_{1-x}(Fe_3O_4)_x$ compounds. *Ceramics International*, *47*(12), 16950–16955. https://doi.org/10.1016/j.ceramint.2021.02.267

Turkoz, M. B., Zalaoglu, Y., Turgay, T., Ozturk, O., Akkurt, B., & Yildirim, G. (2019). Evaluation of key mechanical design properties and mechanical characteristic features of advanced Bi-2212 ceramic materials with homovalent Bi/Ga partial replacement: Combination of experimental and theoretical approaches. *Ceramics International*, *45*(17), 21183–21192. https://doi.org/10.1016/j.ceramint.2019.07.098

Ulgen, A. T., Okur, S., Erdem, U., Terzioglu, C., Turgay, T., Turkoz, M. B., & Yildirim, G. (2023). Development of modulation, pairing mechanism, and slip system with optimum vanadium substitution at Bi-sites in Bi-2212 ceramic structure. *Materials Chemistry and Physics, 307*, Article 128171. https://doi.org/10.1016/j.matchemphys.2023.128171

Vu, L.H., Pham, A.T., Thien, N.D., Nam, N.H., Riviere, E., Pham, Q.N., Man, N.K., Binh, N.T., Hong, N.T.M., Cuong, L.V., Nguyen, T.L., & Tran, D.H. (2023). Enhancements of critical current density in $Bi_{1.6}Pb_{0.4}Sr_2Ca_2Cu_3O_{10+\delta}$ superconductors by additions of SnO_2 nanoparticles. *Ceramics International*, *49*(16), 27614–27621. https://doi.org/10.1016/j.ceramint.2023.06.047